ELSEVIER

Knockdown of *fbxl10/kdm2bb* rescues *chd7* morphant phenotype in a zebrafish model of CHARGE syndrome

CrossMark

Stephanie A. Balow [a], Lain X. Pierce [a], Gabriel E. Zentner [a,d], Patricia A. Conrad [a],
Stephani Davis [e], Hatem E. Sabaawy [e], Brian M. McDermott Jr. [a,b], Peter C. Scacheri [a,c,*]

[a] Department of Genetics and Genome Sciences, Case Western Reserve University, Cleveland, OH, USA
[b] Department of Otolaryngology-Head and Neck Surgery, Case Western Reserve University, Cleveland, OH, USA
[c] Department of Case Comprehensive Cancer Center, Case Western Reserve University, Cleveland, OH, USA
[d] Basic Sciences Division, Fred Hutchinson Cancer Research Center, Seattle, WA, USA
[e] Rutgers Cancer Institute of New Jersey, Robert Wood Johnson Medical School, New Brunswick, NJ, USA

ARTICLE INFO

ABSTRACT

CHARGE syndrome is a sporadic autosomal-dominant genetic disorder characterized by a complex array of birth defects so named for its cardinal features of ocular coloboma, heart defects, choanal atresia, growth retardation, genital abnormalities, and ear abnormalities. Approximately two-thirds of individuals clinically diagnosed with CHARGE syndrome have heterozygous loss-of-function mutations in the gene encoding chromodomain helicase DNA-binding protein 7 (CHD7), an ATP-dependent chromatin remodeler. To examine the role of Chd7 in development, a zebrafish model was generated through morpholino (MO)-mediated targeting of the zebrafish *chd7* transcript. High doses of *chd7* MO induce lethality early in embryonic development. However, low dose-injected embryos are viable, and by 4 days post-fertilization, morphant fish display multiple defects in organ systems analogous to those affected in humans with CHARGE syndrome. The *chd7* morphants show elevated expression of several potent cell-cycle inhibitors including *ink4ab* (*p16/p15*), *p21* and *p27*, accompanied by reduced cell proliferation. We also show that Chd7 is required for proper organization of neural crest-derived craniofacial cartilage structures. Strikingly, MO-mediated knockdown of the jumonji domain-containing histone demethylase *fbxl10/kdm2bb*, a repressor of ribosomal RNA (rRNA) genes, rescues cell proliferation and cartilage defects in *chd7* morphant embryos and can lead to complete rescue of the CHARGE syndrome phenotype. These results indicate that CHARGE-like phenotypes in zebrafish can be mitigated through modulation of *fbxl10* levels and implicate FBXL10 as a possible therapeutic target in CHARGE syndrome.

Introduction

CHARGE syndrome is an autosomal dominant genetic disorder that affects 1 in 10,000–18,000 newborns worldwide (Jongmans et al., 2006; Janssen et al., 2012). CHARGE is an acronym for ocular coloboma, heart defects, atresia of the choanae, retardation of growth and development, genital anomalies, and ear malformations/deafness. The clinical presentation of CHARGE syndrome is highly variable and may include additional features such as cleft lip/palate, cranial nerve dysfunction, kidney anomalies, and rare limb anomalies (Zentner et al., 2010a). Two-thirds of cases of CHARGE syndrome are caused by spontaneous mutation of the gene encoding chromodomain helicase DNA binding protein 7 (CHD7), an ATP-dependent chromatin

remodeler (Vissers et al., 2004; Lalani et al., 2006). Most *CHD7* mutations are nonsense, frameshift, or splice-site, predicted to lead to loss of protein function, and thus CHARGE syndrome is likely due to reduced dosage of CHD7 (Janssen et al., 2012; Bartels et al., 2010). Consistent with haploinsufficiency as the genetic mechanism underlying CHARGE syndrome, mice that are homozygous for *Chd7* null mutations die around embryonic day 10.5, but heterozygous *Chd7* mutants are viable and recapitulate many features of CHARGE syndrome, including heart defects, choanal atresia, postnatal growth retardation, genital abnormalities, abnormal semicircular canals, and cleft palate (Bosman et al., 2005; Hurd et al., 2007).

CHD7 is a member of the CHD family of proteins. Nine proteins comprise this family in vertebrates, and all nine contain tandem N-terminal chromodomains and a central conserved SNF2-like ATPase domain presumed to mediate chromatin remodeling. In addition to the chromodomains and ATPase domain, CHD7 contains two BRK domains of unknown function and a SANT-like domain that may mediate DNA and/or histone binding (Hall and

* Corresponding author at: Department of Genetics and Genome Sciences, 10900 Euclid Ave, Cleveland, OH 44106, USA.
   E-mail address: pxs183@case.edu (P.C. Scacheri).

Georgel, 2007). CHD7 is a nuclear protein and binds to gene enhancer elements and promoters, functioning as a transcriptional co-regulator (Schnetz et al., 2009, 2010; Engelen et al., 2011). CHD7 cooperates with PBAF (polybromo- and BRG1-associated factor-containing complex) to regulate genes important for formation and migration of neural crest, including TWIST and SOX9 (Bajpai et al., 2010). In mouse neural stem cells, CHD7 collaborates with SOX2 to regulate a common set of target genes including Jag1, Gli3, and Mycn. Mutations in these and other genes co-regulated by CHD7 and SOX2 cause clinical malformation syndromes that show some clinical overlap with CHARGE syndrome (Engelen et al., 2011). Thus, it is hypothesized that dysregulated expression of genes normally regulated by CHD7 during development gives rise to the developmental defects observed in CHARGE syndrome.

In addition to its role as a transcriptional regulator in the nucleoplasm, CHD7 localizes to the nucleolus (Zentner et al., 2010b; Kita et al., 2012), where it associates with rDNA and functions as a positive regulator of rRNA transcription. Cell proliferation is tightly coupled to protein synthesis, ribosome biogenesis, and rRNA production (Li et al., 2005; Feng et al., 2010; Pestov et al., 2001; Holzel et al., 2005). Accordingly, siRNA-mediated knockdown of CHD7 in cultured cells suppresses protein synthesis and cell proliferation (Zentner et al., 2010b). Affected tissues from Chd7 mutant mouse embryos also show deficiencies in rRNA levels as well as cell proliferation (Zentner et al., 2010b; Layman et al., 2011; Hurd et al., 2010). These findings raise the possibility that the pathogenesis of CHARGE syndrome is related to that of other human disorders caused by deficiencies in ribosomal biogenesis. Collectively known as the "ribosomopathies", these disorders include Schwachman–Diamond syndrome, dyskeratosis congenita, cartilage hair hypoplasia, Treacher Collins syndrome, and myelodysplastic syndrome (Narla and Ebert, 2010). Despite these discoveries, it remains unclear if the multiple anomalies in CHARGE syndrome are due to dysregulated expression of nucleoplasmic gene targets, rRNA, or the combination of both deficits.

Here, we developed a zebrafish model of CHARGE syndrome through morpholino-mediated targeting of the zebrafish chd7 homolog. At 4 days post fertilization (dpf) chd7 morphant fish show multiple defects in organ systems analogous to those affected in humans with CHARGE syndrome. The defects in the chd7 morphant fish are accompanied by a general deficiency in cell proliferation at the early stages of development, associated with elevated expression of potent cell cycle inhibitors including ink4ab, p21, and p27. Remarkably, reduction of the Fbxl10/Kdm2bb histone demethylase, a negative regulator of rRNA transcription, restores cell proliferation in the chd7 morphants, with concomitant rescue of CHARGE-like phenotypes. Our findings implicate cell proliferation deficiencies in the pathogenesis of CHARGE syndrome, and suggest that elevation of rRNA levels maybe a viable strategy for therapeutic intervention in CHARGE syndrome.

Results

Organization of the zebrafish chd7 gene

The sole zebrafish chd7 gene is located on chromosome 2 (Zv9 Ensembl). Of the five annotated transcripts, one is non-protein coding, two contain only the first two or three exons, and the remaining two are full-length. Both of the full-length transcripts have identical predicted protein coding sequences and have an exon–intron structure similar to that of human CHD7. These full-length transcripts code for a zebrafish Chd7 protein of 3140 amino acids, which is slightly longer than the human homolog of 2997 amino acids. Additionally, the zebrafish Chd7 protein contains a similar complement of protein domains including tandem N-terminal

chromodomains, a central SNF2-like ATPase/helicase domain, and a C-terminal BRK domain (Fig. 1A). The N-termini of zChd7 and hCHD7 are less conserved; however, the remainder of Chd7, including all of the functional domains, is highly similar. Overall, the aligning portion of the zChd7 sequence demonstrates 69% identity to hCHD7 at the amino acid level.

chd7-morpholino gene targeting recapitulates major features of CHARGE syndrome

To model CHD7 haploinsufficiency in zebrafish, an antisense morpholino (MO) was designed to produce a mis-spliced chd7 transcript containing a premature stop codon. Specifically, the MO was targeted to the junction of chd7 intron 15 and exon 16 to induce production of a transcript either missing exon 16 or one including intron 15 (Fig. 1B, upper). We performed RT-PCR analysis using multiple combinations of primers designed to amplify transcripts containing exon 15 mis-spliced to exon 17. However, such transcripts were not detected in chd7 MO-injected embryo, raising the possibility that the chd7 MO blocks splicing of exons 15 and 16, leading to intron inclusion. We therefore performed RT-PCR analysis using multiple primer sets designed to amplify transcript containing an intron 15 inclusion. The expected wild-type transcript was amplified with cDNA from control embryos. The wild-type transcript was also present in chd7 morphant embryos, even upon treatment with high doses of chd7 MO. However, chd7 morphant embryos also expressed a larger transcript, consistent with intron inclusion (Fig. 1C). The levels of the chd7 morphant transcript increased in an MO dose-dependent manner (Fig. 1D). Direct sequence analysis of the morphant transcript cDNA revealed inclusion of intron 15. In silico translation of the morphant transcript predicts mis-incorporation of a premature stop codon at 1383 amino acids past the first codon (Fig. 1B, lower), presumably leading to degradation of the morphant chd7 message via nonsense-mediated decay.

The chd7 morphants exhibited CHARGE-like defects in an MO dose-dependent manner. Specifically, high doses of chd7-MO (5–10 ng) induced lethality within 24 h post-fertilization (hpf), reminiscent of embryonic lethality observed in homozygous null Chd7 mice (Bosman et al., 2005; Hurd et al., 2007). Low-doses of chd7-MO (2.5 ng) yielded viable fish that were indistinguishable from wild-type and control-injected embryos at 3 days post-fertilization (dpf). However, multiple defects were apparent at 4 dpf (Fig. 2A–D). Approximately 95% of low-dose chd7-MO injected embryos showed an abnormal phenotype (Fig. 2E–L). chd7 morphant fish developed defects in organs analogous to those affected in humans and mice with heterozygous CHD7 mutations (Supplemental Table 1). Defects included pectoral fin hypoplasia (~60%), eye abnormalities (70%), and abnormalities in both otolith morphology and number (approximately 25% and 10% respectively) (Fig. 2E–L). Moreover, ~60% of chd7 morphants presented with heart defects including pericardial edema, weak heartbeat with reduced circulatory flow, and occasionally a lack of proper heart tube folding. Importantly, 64% of chd7 morphants also exhibited craniofacial defects involving the nasal region and jaw (Fig. 3A–B). None of these defects were apparent upon injection of a chd7 MO containing a 5-bp mismatch to the endogenous chd7 gene, indicating that the observed defects are specific to chd7 targeting. To further verify specificity, we tested a second splice-blocker chd7 MO, and a third chd7-MO designed to block translation. Both the second splice-blocker and chd7-translation blocker yielded similar phenotypes to that seen with the original splice blocker MO, although the translation blocker yielded more severe heart defects, and ear defects were observed at a higher frequency. No aspects of chd7 morphant phenotype were rescued upon co-injection of chd7 and p53 morpholinos, indicating that the observed defects in the chd7 morphants are unlikely to be related to
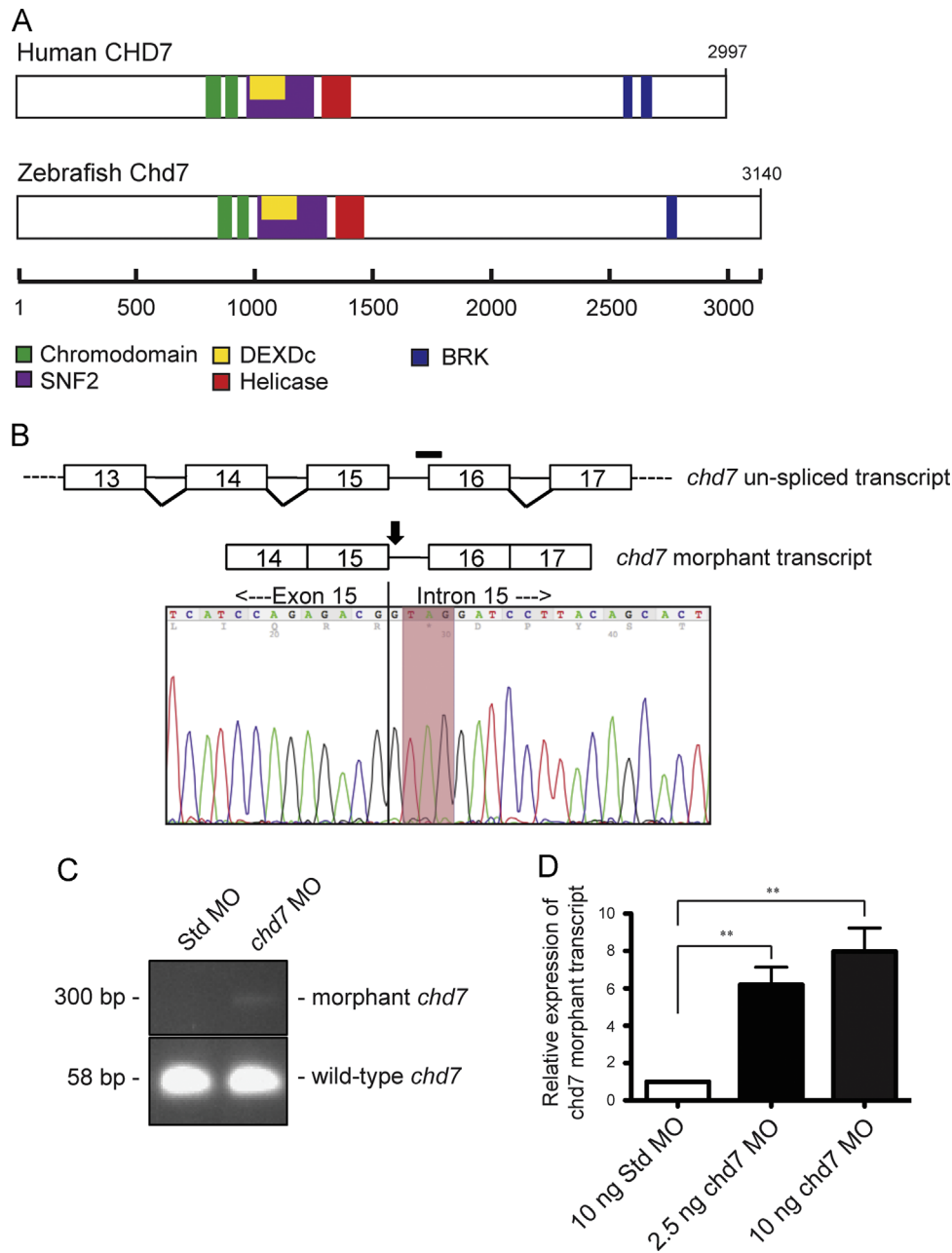
Fig. 1. Morpholino targeting of the zebrafish *chd7* RNA induces an aberrant transcript. (A) Schematic of the human CHD7 and zebrafish Chd7 proteins with the location of the predicted protein domains. (B) Schematic of the zebrafish un-spliced *chd7* transcript (upper) and the exon/intron splice site targeted by the *chd7* morpholino (black bar). Schematic of the *chd7* morphant transcript (lower) with the location of the predicted induced nonsense mutation (black arrow). Chromatogram of the sequenced morphant transcript PCR product reveals a nonsense mutation (red highlight). (C) Agarose gel with the amplified PCR products of both wild-type and morphant *chd7* transcripts from Std control morphants and *chd7* morphants. (D) Graph of qRT-PCR data quantifying the expression of the *chd7* morphant transcript. Error bars represent standard error of the mean (SEM) ($n=4$). Significance was determined by a Student's two-tailed *t*-test and significant *p*-values are noted $p < 0.01$ (**). (For interpretation of the references to color in this figure legend, the reader is referred to the web version of this article.)

non-specific MO-mediated cell death. Lastly, we note that the observed phenotype resembles that reported in a separate study in which the *chd7* gene was targeted using a different splice-blocker MO (Jacobs-McDaniels and Albertson, 2011; Patten et al., 2012). Overall, the *chd7* morphants displayed defects in many of the same organs affected in humans and mice with *CHD7* mutations, including the ear, eye, heart, craniofacial region, and limbs. Thus, the requirement for CHD7 in the development of these organs appears to be conserved between mice, humans, and zebrafish, and suggests that MO-mediated targeting of *chd7* creates a suitable system to examine Chd7 function in development.

chd7 morphants develop defects in neural crest-derived craniofacial cartilage

Early zebrafish craniofacial structure is dependent on proper migration of the multipotent cranial neural cells from the neural tube into the pharyngeal arches. These cells differentiate to form several tissues of the developing cranium such as the cranial nerves, bones, and cartilage (Knight and Schilling, 2006). Based on these findings and published studies implicating a deficiency in neural crest cell migration in CHARGE syndrome (Bajpai et al., 2010; Patten et al., 2012), we performed a detailed morphological analysis of craniofacial cartilage in
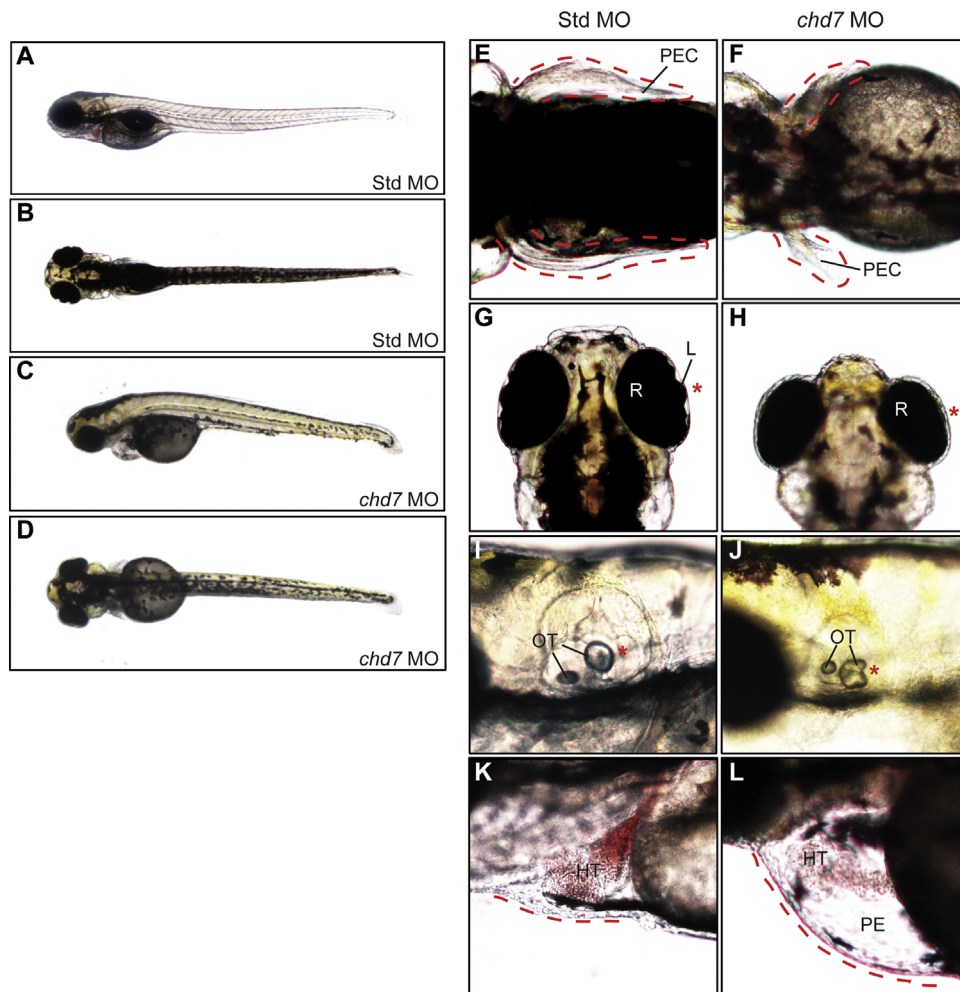
Fig. 2. Zebrafish *chd7* targeting results in CHARGE-like phenotypes. Whole-embryo lateral (A, C) and dorsal (B, D) views of representative Std control and *chd7* morphant embryos at 4 dpf. The *chd7* morphants display pectoral fin defects (E–F), eye abnormalities including under-developed or missing anterior eye structures (G–H), changes in otolith morphology (I–J), and pericardial edema (K–L). Missing or abnormal structures are highlighted with an asterisk (*) and/or dashed line. Structures are also highlighted in Std morphants for comparison. HT=heart, L=lens, OT=otolith, PE=pericardial edema, PEC=pectoral fin, and R=retina.

low-dose *chd7* morphant embryos. Compared to Standard MO-injected controls, *chd7* morphants showed a wide range of craniofacial cartilage abnormalities (Fig. 3F–G). In approximately 50% of *chd7* morphants, the first pharyngeal arch comprising Meckel's cartilage and the palatoquadrate were morphologically normal. However, Meckel's cartilage was located posteriorly to that observed in control morphants. In addition, the ceratobranchial cartilages were absent, and the ceratohyal was malformed (less V-shaped) compared to controls. In the majority of *chd7* morphants, the ceratobranchial arches were undetectable at this resolution. However, microscopic analysis of sagittal sections revealed that the first ceratobranchial arch was occasionally present (Supplemental Fig. 1). In more severely affected *chd7* morphants, the only craniofacial cartilage structure observed was a severely underdeveloped neurocranium with malformed parachordal and trabecula cranii cartilages. Interestingly, parachordal and trabecula cranii cartilages are partially derived from mesoderm, while the more anterior cartilage structures that were typically absent in the severe *chd7* morphants are mostly derived from neural crest (Kague et al., 2012). These results suggest that *chd7* plays a critical role in the formation of cranial neural crest-derived cartilage tissues.

Chd7 is required for normal cellular proliferation during zebrafish development

In E9.5–E10.5 mouse embryos, haploinsufficiency of CHD7 is associated with reduced proliferation of olfactory neural stem cells and cells of the otic epithelium and ganglion (Layman et al., 2011; Hurd et al., 2010). Moreover, we previously showed that siRNA-mediated knockdown of CHD7 in cultured cells attenuates their proliferation (Zentner et al., 2010b). These proliferative deficiencies occur without concomitant increases in cell death, indicating that CHD7 regulates cell proliferation and not apoptosis. We tested for proliferative defects in the *chd7* morphants through immuno-fluorescence analysis of phosphorylated histone H3 at serine 10 (P-H3), a marker of mitosis (Fig. 4A–B). Compared to control embryos, the total area positive for cellular P-H3 expression in *chd7* morphants (25 hpf) was reduced by 37% in the anterior region of the embryo (Fig. 4C). In addition, counts of P-H3 immuno-positive cells showed a 47% reduction in the total number of proliferating cells in *chd7* morphants compared to controls (Fig. 4D–E). A reduction in the number of proliferating cells was detected not only in the anterior region of the embryo (Fig. 4D), where *chd7* levels are high at this stage of development, but also the tail region (Fig. 4E), where *chd7* levels are low. Zebrafish *chd7* expression is ubiquitous in early development and becomes more anteriorized around 3 dpf (Rauch et al., 2003). Thus, the observed proliferative deficiencies are probably related to Chd7's role during early development, prior to the time at which *chd7* expression is restricted to the anterior region of the zebrafish embryo.

Similar to the findings in mice and cultured cells, the proliferative defects in the *chd7* morphants occurred in the absence of
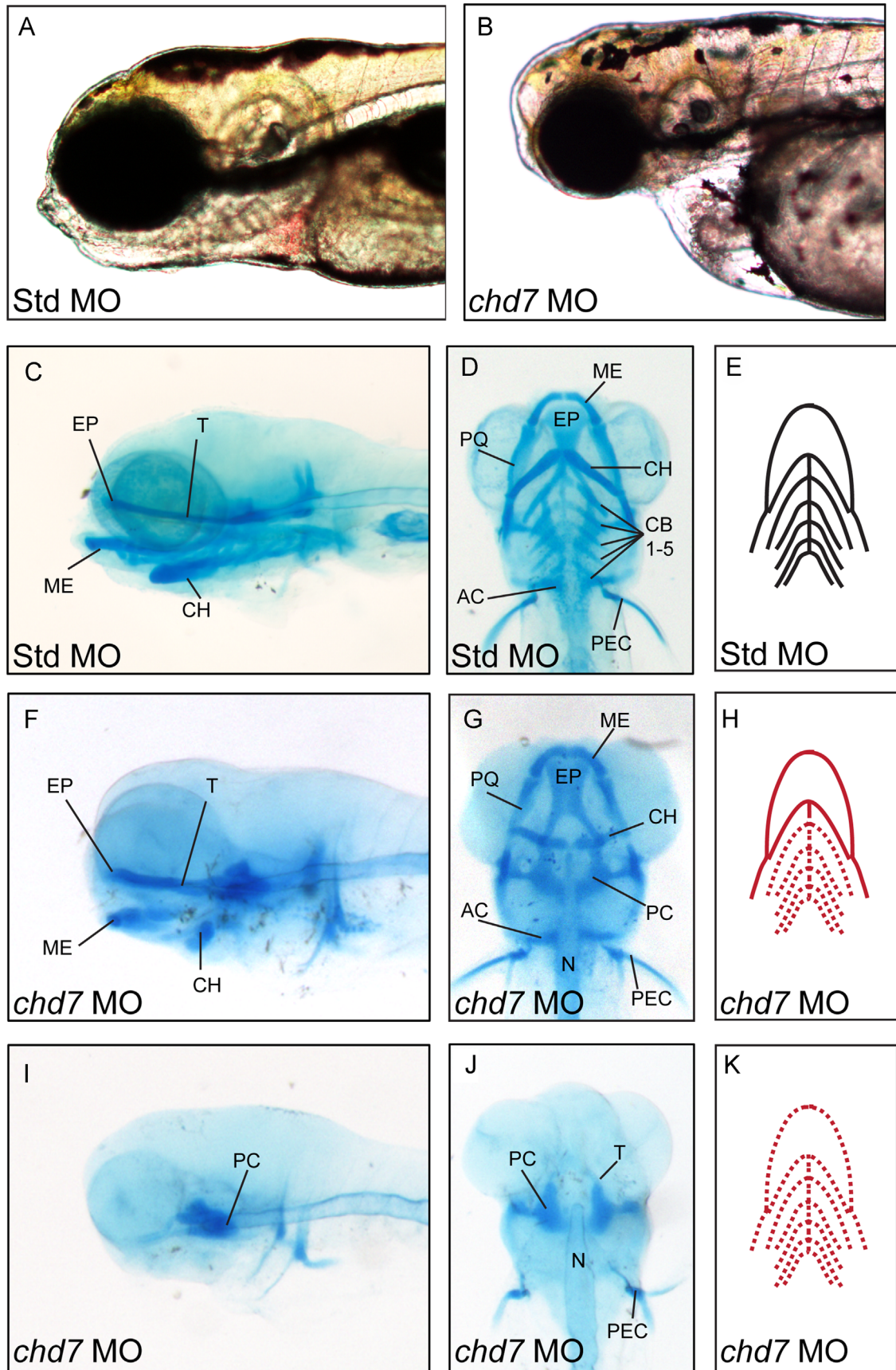
Fig. 3. *chd7* morphants display variable defects in craniofacial cartilage development. (A–B) Bright-field lateral views of representative Std control morphants and *chd7* morphants at 4 dpf. (C–D) Lateral and ventral views of Std morphants with wild-type craniofacial cartilage structures at 4 dpf. (F–G) Representative lateral and ventral views of the average *chd7* morphant phenotype and is categorized as underdeveloped. The ceratohyal cartilages of the *chd7* morphant are malformed and form a more linear shape. The five ceratobranchial cartilages were also undetectable with Alcian blue staining. (I–J) Lateral and ventral views of a severe *chd7* morphant phenotype detected a highly underdeveloped neurocranium with the anterior and branchial arches absent. (E, H, K) Schematic views of the zebrafish craniofacial cartilage excluding the neurocranium. A solid red line indicates that the structure is present but malformed; while, a dashed red line indicates that the structure is absent. AC=auditory capsule, CB=ceratobranchial, CH=ceratohyal, EP=ethmoid plate, ME=Meckel's cartilage, N=notochord, PC=parachordal, PEC=pectoral fin, PQ=palatoquadrate, and T=trabeculacranii. (For interpretation of the references to color in this figure legend, the reader is referred to the web version of this article.)

apoptosis, as determined through TUNEL-assays (data not shown). The proliferative deficiencies were accompanied by elevated expression of potent cell-cycle inhibitors, including *p21*, *p27*, and *ink4ab* (the zebrafish homolog of both *p15* and *p16*) (Sabaawy et al., 2006) (Fig. 4F–H). Because we have previously shown that decreases in rRNA correlate with reduced proliferation, we also quantified the levels of 45S pre-rRNA, the product of Pol I transcription of rDNA that is ultimately processed into the mature 18S, 5S, and 28S ribosomal subunits (Zentner et al., 2010b; McStay and Grummt, 2008). No significant differences in pre-rRNA levels were detected between *chd7* morphants and controls, even in embryos injected with high doses of *chd7* MO (Fig. 4I). Thus, either Chd7 does not regulate rRNA in the zebrafish, or the effect is restricted to specific cell types or other stages of development. Overall, these findings indicate that Chd7 is required for normal cellular proliferation in the developing zebrafish embryo, although it is currently not clear from these data that the effect is mediated through rDNA regulation.

Fbxl10 regulates rRNA levels during zebrafish embryogenesis

Cell proliferation rates are tightly coupled to ribosomal RNA levels. Though our results were inconclusive as to whether zebrafish Chd7 regulates rRNA, we set out to modulate rRNA levels in *chd7* morphants, reasoning that this might restore the proliferative deficiencies. To achieve this, we chose to knockdown the homolog of a known repressor of rRNA genes in mammals: FBXL10 (also known as NDY1, JHDM1B, and KDM2B). FBXL10 is a jumonji domain-containing histone demethylase that represses rRNA genes in the mammalian nucleolus, suppressing cell proliferation (Frescas et al., 2007). Other studies contradict these findings, suggesting that FBXL10 increases proliferation by directly suppressing cell-cycle inhibitors in the nucleoplasm, including *p15Ink4b*, *p16Ink4a*, and *p19Arf* (He et al., 2008; Tzatsos et al., 2009, 2011). Similarly to *chd7*, *fbxl10* (*kdm2bb*) is expressed ubiquitously throughout early zebrafish embryogenesis. By 4 dpf, *fbxl10* expression is restricted to the anterior embryo including the retina and central nervous system
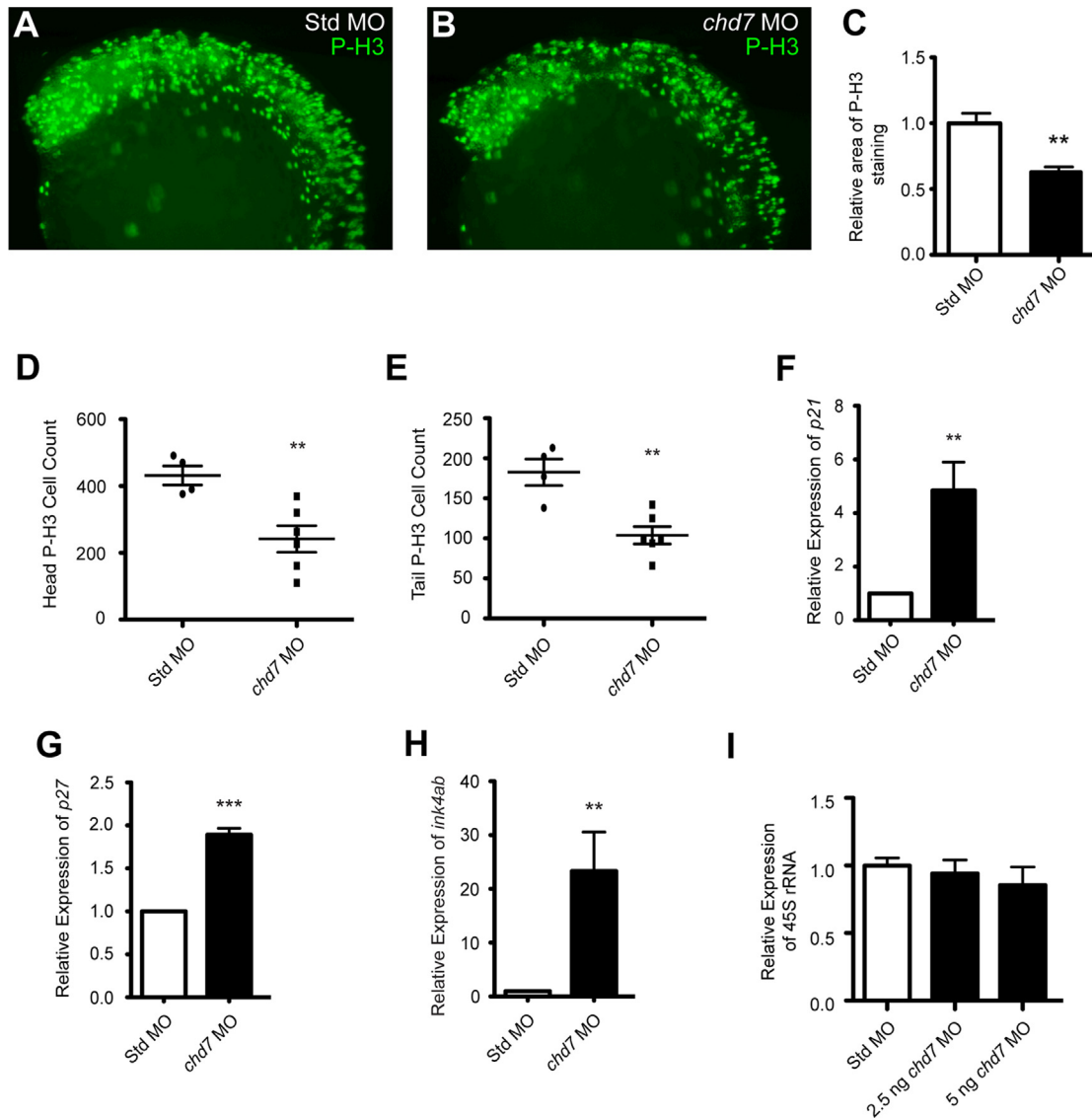

Fig. 4. *chd7* targeting impairs cell proliferation. (A–B) Lateral views of representative P-H3 stained zebrafish morphants at 25 hpf. (C) Quantification of the area occupied by P-H3 positive cells in *chd7* morphants relative to P-H3 positive cells in Std morphants ($n=5$–6). (D–E) Graphs of P-H3 positive cell counts taken from confocal images of both the head and tail regions of Std and *chd7* morphants ($n=4$–6). (F–H) Graphs of qRT-PCR data measuring gene expression of several cell cycle regulator genes at 25 hpf in *chd7* morphants relative to Std morphants ($n=5$–6). (I) Expression of pre-rRNA in *chd7* morphants at two separate morpholino dosages relative to Std morphants at 8 hpf ($n=3$). All error bars represent SEM. Significance for all graphs was determined with a Student's two-tailed *t*-test and significant values are noted $p < 0.01$ (**) and $p < 0.001$ (***).

(Thisse and Thisse, 2004). Using a splice-blocker morpholino, we knocked down *fbxl10* transcript levels by 35% to 50% (Fig. 5A–B). When 5 ng of MO was injected, the *fbxl10* knockdown yielded viable fish without an obvious gross morphological abnormalities or defects in craniofacial cartilage structures (Fig. 5C–D, Supplemental Fig. 2). Additionally, *fbxl10* knockdown did not impact cell proliferation (Fig. 5E–G). However, higher doses of *fbxl10* morpholino induced early embryonic lethality by 24 hpf. Also, *chd7* expression was also found to be normal in *fbxl10* morphants when measured by qRT-PCR (not shown). We next tested if Fbxl10 regulates rRNA in the nucleolus or cell cycle genes in the nucleoplasm. 45S pre-rRNA levels were 30% higher in embryos injected with *fbxl10*-MO than control embryos (Fig. 5H). *ink4ab* levels were not significantly different between controls and *fbxl10* morphants (Fig. 5I). These results support the reported mammalian function of Fbxl10 as a repressor of rRNA genes in the nucleolus.

Rescue of chd7 morphant phenotype upon knockdown of fbxl10

Having established that Fbxl10 represses rRNA levels in the fish, we tested the effects of knocking down both *fbxl10* and *chd7*, through co-injection of *chd7* and *fbxl10* morpholinos. Co-injection of *fbxl10*-MO and the *chd7*-translation blocker MO induced embryonic lethality within 24 hpf. However, co-injection of *fbxl10*-MO with the *chd7* splice blocker MO suppressed the morphological defects induced by *chd7* morpholino alone. Specifically, co-injection of *chd7* and *fbxl10* morpholinos reduced the penetrance of pericardial edema (13% from
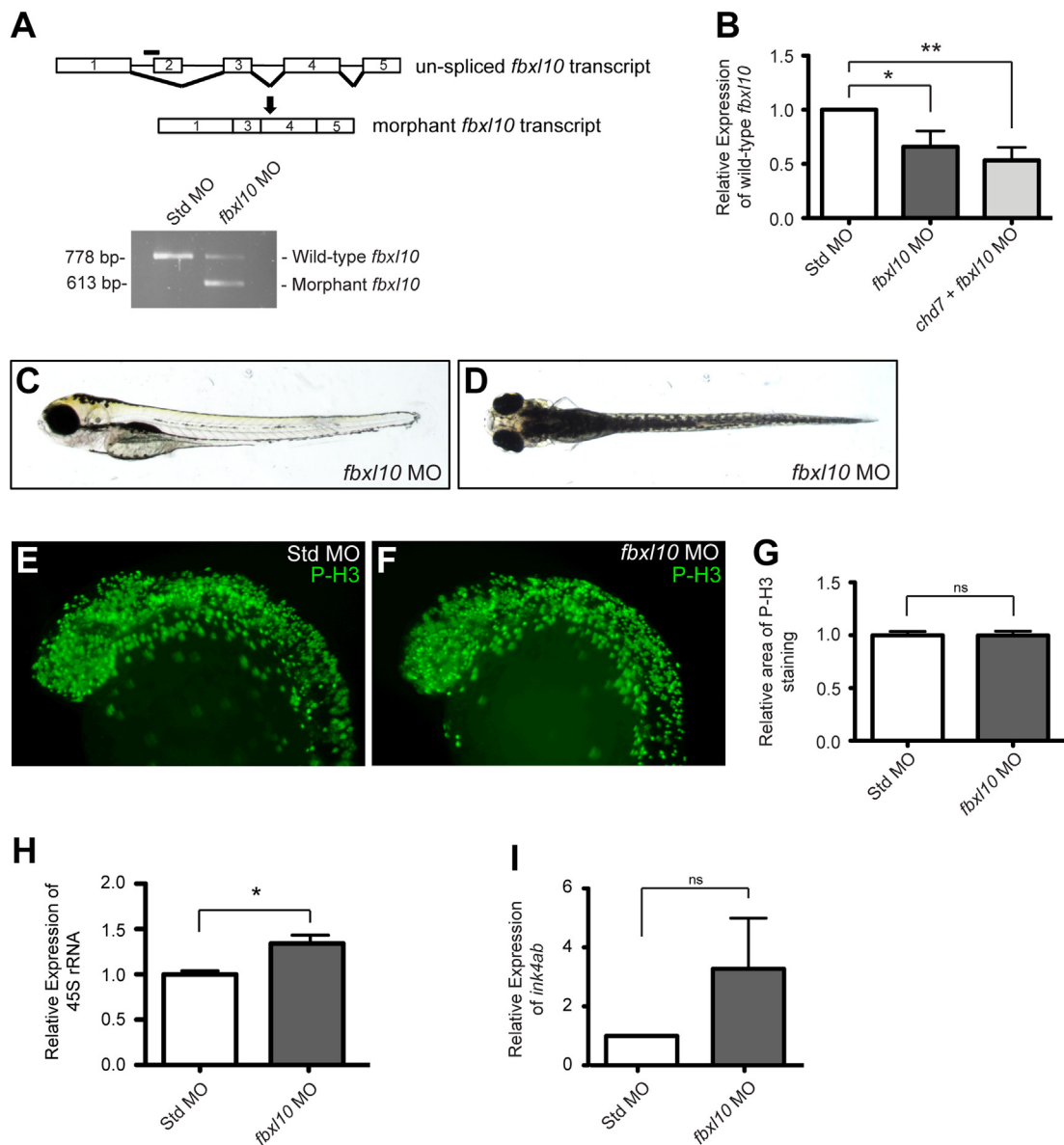

Fig. 5. Targeting of zebrafish *fbxl10* transcript modulates pre-rRNA expression. (A) Schematic of the un-spliced *fbxl10* transcript and the location of the *fbxl10* morpholino (black bar). Injection of the morpholino results in an exclusion of exon 2 in the mature *fbxl10* transcript and is predicted to induce a nonsense mutation (black arrow). Exclusion of exon 2 in the *fbxl10* morphant transcript was confirmed by PCR. (B) Graph of qRT-PCR data measuring the expression of wild-type *fbxl10* relative to the expression in Std control morphants at 8 hpf ($n=4$). (C–D) Representative lateral (C) and dorsal (D) bright-field images of *fbxl10* morphants at 25 hpf. (E–F) Lateral views of representative P-H3 stained zebrafish morphants at 25 hpf. (G) Quantification of the area occupied by P-H3 positive cells in *fbxl10* morphants relative to P-H3 positive cells in Std morphants ($n=12$–13). (H) Graph of qRT-PCR expression data for 45S pre-rRNA relative in *fbxl10* morphants relative to Std morphants ($n=4$). (I) Graph of qRT-PCR data measuring *ink4ab* expression relative to Std morphants ($n=6$).Error bars in all graphs represent SEM. Significance determined by a Student's two-tailed *t*-test and significant values are noted $p < 0.05$ (*) and $p < 0.01$ (**).

58%), eye abnormalities (11% from 73%), pectoral fin defects (8% from 55%), craniofacial defects (27% from 64%), and otolith abnormalities (0% from 25%) (Fig. 6A). In addition to the improvement of gross morphology discussed above, we also observed a significant

restoration in overall head size in the *chd7/fbxl10* double morphants compared to the *chd7* morphant (Supplemental Fig. 3).

Forty-six percent of co-injected morphants showed restoration of the craniofacial cartilage to wild-type or near wild-type morphology
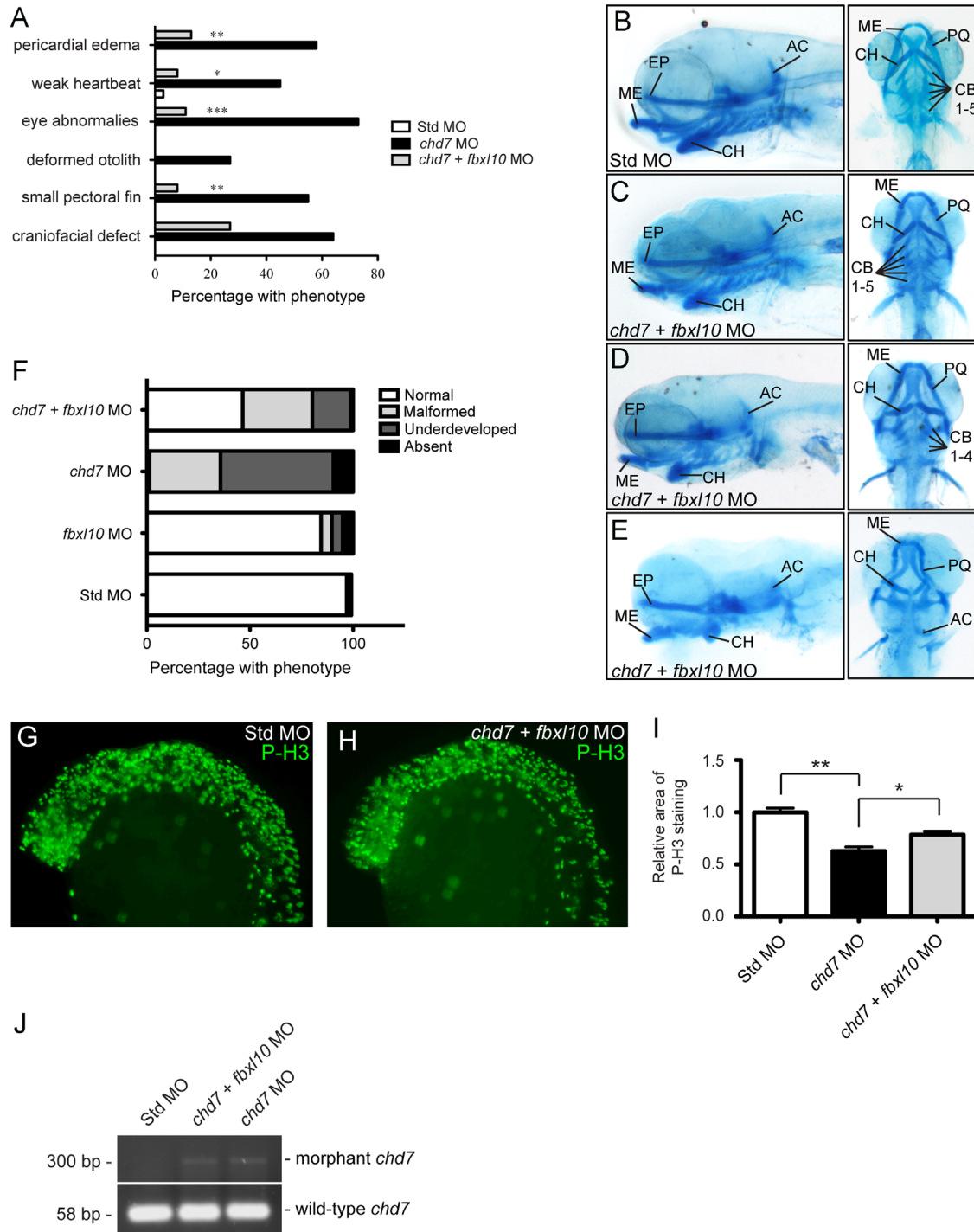

Fig. 6. Modulation of fbxl10 expression rescues CHARGE-like phenotypes and improves cellular proliferation defects. (A) Graph of the percentage of observed CHARGE-like phenotypes across the different zebrafish morphants. Significance was determined by chi-square tests. (B–E) Lateral and ventral views of representative cartilage staining in the *chd7/fbxl10* double morphants compared to controls (B) at 4 dpf including morphants with normal phenotypes (C), mild malformations of the ceratohyal (D), and *chd7/fbxl10* double morphants with severe ceratohyal malformations and ceratobranchial cartilage were undetectable (E). (F) Graph of the frequency of the observed craniofacial cartilage phenotypes in the developing zebrafish. Zebrafish were categorized on the severity of the craniofacial cartilage defect. "Malformed" morphants had all cartilages present but displayed morphological changes in the ceratohyal. "Underdeveloped" morphants had no detectable ceratobranchial arches in addition to a malformed ceratohyal. A morphant was categorized "Absent" with no detectable anterior and branchial arches. A highly underdeveloped neurocranium was present in these morphants. (G–H) Lateral views of representative P-H3 stained zebrafish Std and *chd7/fbxl10* morphants at 25 hpf. (I) Quantification of the area occupied by P-H3 positive cells in *chd7* morphants (re-plotted from Fig. 4C) and *chd7/fbxl10* morphants relative to P-H3 positive cells in Std morphants (n=7). (J) Representative image of the amplified PCR products of both wild-type and morphant *chd7* transcripts from 8 hpf across the panel of morphants. Significant *p*-values in all graphs are noted $p < 0.05$ (*), $p < 0.01$ (**), $p < 0.001$ (***). AC=auditory capsule, CB=ceratobranchial, CH=ceratohyal, EP=ethmoid plate, ME=Meckel's cartilage, and PQ=palatoquadrate.

with only minor malformations in the second pharyngeal arch (Fig. 6B–C, Supplemental Fig. 4A). Compared to the single *chd7* morphants (Fig. 3F–G), the *chd7/fbxl10* morphants had more anteriorly developed Meckel's cartilage, a wild-type or near wild-type ceratohyal morphology, and all ceratobranchial arches were detectable upon Alcian blue staining. The remaining 54% showed craniofacial cartilage abnormalities similar to those observed in *chd7* single morphants, but in general, these abnormalities were less severe than those seen in the single *chd7* morphants (Fig. 6D–F). For example, the *chd7/fbxl10* double morphants had a similar proportion of morphants categorized to be malformed compared to the *chd7* single morphants due to more linear ceratohyal morphologies (Fig. 6D, Supplemental Fig. 4B). However, only a small proportion of the *chd7/fbxl10* double morphants were scored as underdeveloped with both an inverted ceratohyal cartilage and undetectable ceratobranchial arches (Fig. 6E, Supplemental Fig. 4C). This indicates a significant restoration of the ceratobranchial arches in the double morphants. The craniofacial cartilage structures in the majority of single *fbxl10* morphants injected in parallel were again indistinguishable from the standard-MO controls (Fig. 6F).

We also analyzed cell proliferation through quantitative analysis of P-H3 immuno-positive cells in morphant embryos. Relative to controls, the percentage of mitotic cells within measured areas increased from 63% in *chd7* single morphants to 78% in co-injected embryos (Fig. 6G–I). Importantly, these percentages reflect average counts from multiple co-injected embryos, from which the degree of rescue was variable. In fact, analysis of individual P-H3 immuno-stained embryos showed complete to near-complete restoration of cell proliferation in approximately two-thirds of all embryos analyzed ($n=29$). Overall, these data indicate that knockdown of *fbxl10* can mitigate *chd7*-morphant phenotypes in zebrafish. Importantly, co-injected embryos retained the *chd7* morphant transcript, indicating that the effects of Fbxl10 depletion genuinely trump those of Chd7 depletion, and that rescue is not simply due to loss of the *chd7* morphant transcript (Fig. 6J).

Analysis of rRNA and cell cycle genes in fbxl10/chd7 double morphants

To gain insights into the mechanism underlying the *fbxl10*-mediated rescue, we compared the levels of rRNA, *p21*, *p27*, and *ink4ab* in *fbxl10/chd7* co-injected morphant embryos to those in *chd7* single morphants and standard-injected embryos. These
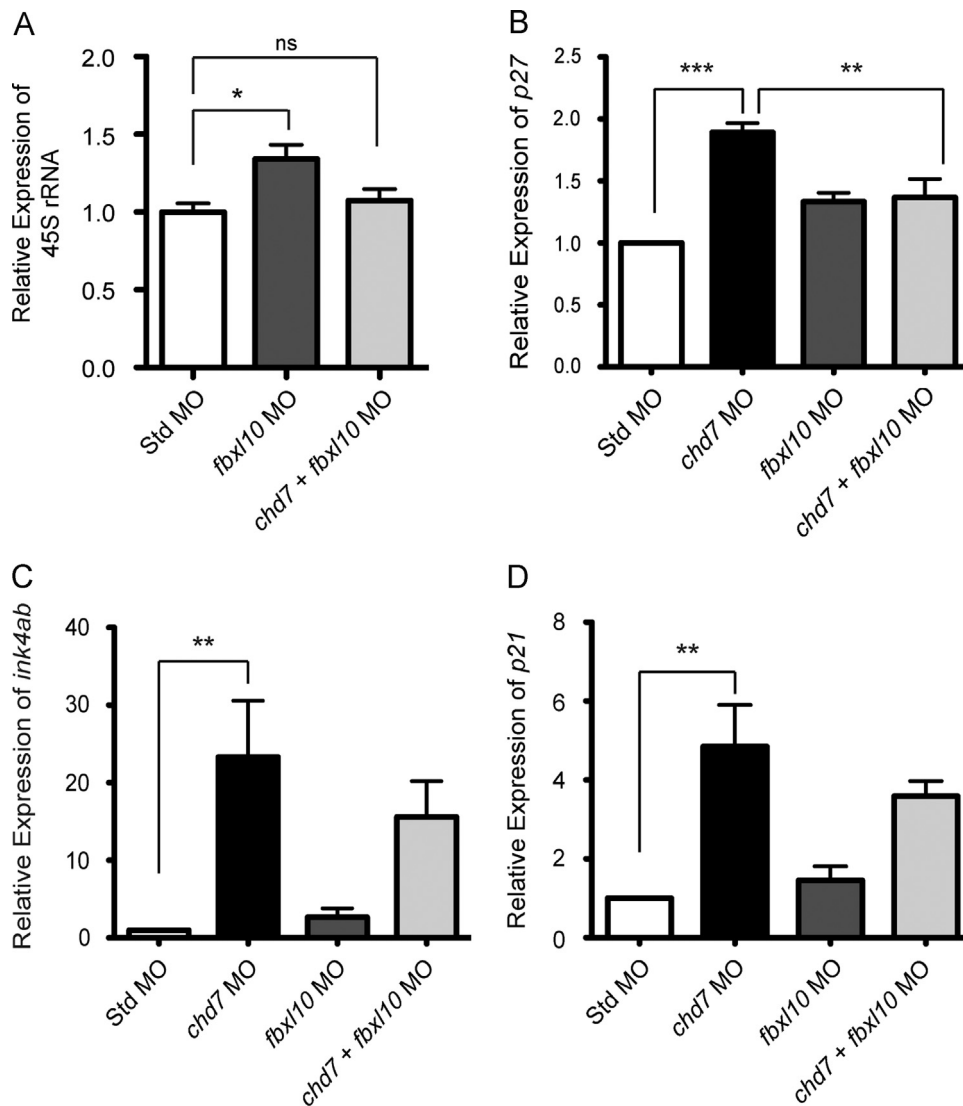

Fig. 7. Gene expression changes in cell-cycle regulators in *chd7/fbxl10* double morphants. (A) Expression of pre-rRNA in *chd7/fbxl10* double morphants and *fbxl10* single morphants (re-plotted for comparison from Fig. 5H) relative to Std morphants at 8 hpf ($n=3$). (B–D) Graphs of qRT-PCR data measuring gene expression of several cell cycle regulator genes at 25 hpf across the panel of morphant embryos relative to Std morphants ($n=5$–6). Expression data for *chd7* morphants re-plotted here from Fig. 4F–H for comparison. Error bars represent SEM. Significance for all graphs was determined with a Student's two-tailed *t*-test and significant values are noted $p < 0.05$ (*), $p < 0.01$ (**), $p < 0.001$ (***).

experiments are inherently difficult to analyze for several reasons. First, 46% of co-injected embryos show rescue by 4 dpf, and, at the 25 hpf time point at which embryos are collected to perform the assay, one cannot distinguish rescued embryos from those that will fail to show rescue. In addition, embryos must be pooled to obtain sufficient quantities of RNA for the analysis. Nonetheless, we found that pre-rRNA levels were similar between co-injected and control-injected embryos, indicating that the *fbxl10*-mediated increases in rRNA are attenuated through targeted knockdown of *chd7* (Fig. 7A). Thus, even though reduced rRNA levels were not detected in the *chd7* single morphants, elevated rRNA levels in the *fbxl10* morphants are clearly attenuated upon knockdown of *chd7*, suggesting that Chd7's role as a positive regulator of rRNA may be context specific. *p27* levels, elevated in the *chd7* single morphants, were also attenuated upon co-injection of *fbxl10* and *chd7* morpholinos (Fig. 7B). *p21* and *ink4ab* levels in *chd7* single morphants were not significantly different from co-injected embryos (Fig. 7C–D). However, these results reflect transcript levels measured from pooled co-injected embryos, of which 46% were rescued and 54% remained morphant. Thus, the levels of *p21* and *ink4ab* shown in the plots, which are clearly trending downward, may be much lower in the 46% of embryos that were rescued. Based on these findings, we propose that elevated rRNA levels, induced upon knockdown of *fbxl10*, leads to suppression of cell cycle inhibitors activated upon *chd7* targeting, thereby alleviating the *chd7*-associated cell proliferation defect.

Discussion

To study the role of Chd7 during development, we generated a zebrafish model of CHARGE syndrome through MO-mediated gene targeting. The *chd7* morphant phenotype is highly MO dose-dependent, with high doses leading to early embryonic lethality and lower doses yielding viable fish with craniofacial defects as well as malformations of the eye, heart, otoliths, and pectoral fins. The *chd7* morphants also show cranial cartilage abnormalities, consistent with a defect in developing neural crest, the proposed cell type of origin for many of the anomalies observed in CHARGE syndrome patients (Bajpai et al., 2010; Patten et al., 2012; Siebert et al., 1985; Sanlaville et al., 2006; Randall et al., 2009). The *chd7* morphant embryos also display widespread deficiencies in cellular proliferation, accompanied by elevated levels of potent cell-cycle inhibitors. Remarkably, the gross morphological alterations, cartilage abnormalities, and cell proliferation deficiencies that define the *chd7* morphant phenotype are all restorable with knockdown of Fbxl10, a repressor of rRNA. We propose that the mechanism of rescue is due to suppression of cell cycle inhibitors that are activated upon *chd7* targeting, possibly through global modulation of rRNA levels.

To date, zebrafish, frogs, and mice have been used to study the role of CHD7 in development (Bosman et al., 2005; Hurd et al., 2007; Bajpai et al., 2010; Patten et al., 2012; Layman et al., 2009; Tian et al., 2012). The overall phenotype and the organ systems affected in the *chd7* morphants reported here are consistent with those previously observed in the other models (Supplemental Table 1). For example, defects in neural crest development and malformed craniofacial cartilage structures were previously reported in both zebrafish and frogs. Similarly to our zebrafish model, the frog model also shows facial width compression (Bajpai et al., 2010). As in the previously described zebrafish, frog, and mouse models, *chd7* morphants described here show eye, heart, and otolith abnormalities. However the specific anomalies described vary somewhat between the models. With respect to the eyes for example, our zebrafish models show an underdeveloped lens, the previously described zebrafish models show retinal

disorganization, the frog models develop colobomas, and the mouse models present with keratoconjunctivitis sicca (Bosman et al., 2005; Bajpai et al., 2010; Patten et al., 2012; Tian et al., 2012). The underlying basis for these differences is not known, but interestingly, this phenotypic variability is highly reminiscent of that seen among human patients with CHARGE syndrome and warrants further study.

To better understand the contribution of the proliferative deficiencies to the overall phenotype of the *chd7* morphants, we knocked down the levels of *fbxl10/kdm2bb*, a histone demethylase that normally suppresses cell proliferation and has a similar spatiotemporal expression pattern to *chd7* (Rauch et al., 2003; Frescas et al., 2007; He et al., 2008; Tzatsos et al., 2009; Thisse and Thisse, 2004). To our knowledge, this is the first report of a zebrafish *fbxl10* morphant model, and the first report that *fbxl10* modulates rRNA levels in the zebrafish. Fifty percent reduction of *fbxl10* did not yield any gross morphological abnormalities. However, more substantial decreases of *fbxl10* induced early embryonic lethality by the end of the segmentation period (24 hpf). This phenotype is somewhat reminiscent of that observed in *Fbxl10* mutant mice. Specifically, *fbxl10* heterozygotes develop normally, while *fbxl10*-null homozygotes die during late embryogenesis or shortly after birth (Fukuda et al., 2011).

It has been demonstrated in several model systems that decrease in *CHD7* levels impair cellular proliferation in multiple cell types (Zentner et al., 2010b; Layman et al., 2011). Our studies not only corroborate these findings, but also implicate proliferative deficiencies as the basis for the developmental anomalies observed in the zebrafish model of CHARGE syndrome. The rescue of a multiple congenital anomaly syndrome caused by a deficiency in rRNA biogenesis is not unprecedented. Treacher-Collins Syndrome (TCS) is a congenital disorder of craniofacial development caused by mutations in *TCOF1* and *POLR1D* (Edwards et al., 1997; Gladwin et al., 1996; Dauwerse et al., 2011). These mutations lead to reduced rRNA biogenesis, and similarly to CHARGE syndrome, neural crest is implicated as the cell type of origin for most of the associated anomalies in TCS. In mouse models of TCS, impaired ribosome biogenesis triggers the nucleolar stress response, activating p53 and leading to proliferative deficiencies and apoptosis of neural crest cells. Moreover, inhibition of p53 blocks neural crest apoptosis and rescues the craniofacial defects (Jones et al., 2008). In our study, several genes associated with the nucleolar stress response, including *p21*, *p27* and rRNA itself, responded upon MO-targeting of *chd7* and *fbxl10*. These findings lead us to hypothesize that the cell proliferation defects observed in the *chd7* morphants are due to activation of the nucleolar stress response, like in TCS. However, MO-mediated knockdown of p53 failed to rescue the chd7 morphant phenotype. Additionally, we previously showed that proliferative deficiencies induced upon knockdown of *CHD7* in cultured cells were accompanied by changes in the levels of rRNA and *p21*, but not *p53* (Zentner et al., 2010b). Thus, if the nucleolar stress response is the basis of the proliferative defect seen in the *chd7* morphants, and the mechanism of rescue is due to suppression of the nucleolar stress response, it is likely to be p53-independent.

Together with the proposed role for CHD7 as a regulator of rRNA transcription in the nucleolus, the multiple anomalies in CHARGE syndrome are thought to due to insufficiencies in cell specification and proliferation during development. Our findings in the zebrafish suggest that restoring the cell proliferative deficiencies at the early stages of embryogenesis, even in the context of the other cellular deficits, could be sufficient to attenuate or altogether bypass the developmental defects associated with *CHD7* mutation. Our studies lay the foundation to test this hypothesis in higher vertebrates, either through targeted modulation of FBXL10 or other genes that regulate rRNA levels, or genes that directly regulate the cell cycle. It is also noteworthy that histone demethylases are particularly amenable to targeting with small-molecule inhibitors (Cole, 2008; Lohse et al., 2011).

If the findings here on Fbxl10 are validated in higher vertebrates, we might be able to tap into this growing area of therapeutic research for application to CHARGE syndrome.

Methods

Zebrafish maintenance

Wild-type Tuebingen (TÜ) zebrafish (*Danio rerio*) embryos were raised at 28 °C. The zebrafish were raised on 14-hour light cycle and 10-hour dark cycle.

Protein sequence comparison

Human CHD7 (NP_060250.2) and zebrafish Chd7 (ENSDART 00000016208) protein sequences were aligned using the NCBI BLAST blastp suite to determine the degree of amino acid overlap between the two sequences (Altschul et al., 1997). To retrieve the predicted domain composition of each protein sequence, we used the NCBI Conserved Domain Database (Marchler-Bauer et al., 2011).

Morpholino design and injection

A splice-blocking morpholino, 5′-ACCTACAATGAAGGAAATAGG-CCGT-3′, a 5-bp mismatch control morpholino, 5′-ACGTAGAATCAG-CAAATACGCCGT-3′, a second confirmation splice-blocking morpholino, 5′-TGTGCCTGGAGGCAACAGCACAAAC-3′, and a translation-blocking morpholino, 5′-GGCTCATCATGCCTGGGTCAGCCAT-3′ were designed against the zebrafish *chd7* transcript (ENSDART000000 16208). To reduce *fbxl10* expression, we used a splice-blocking morpholino designed against the zebrafish *fbxl10* transcript (ENSDART 00000102530), 5′-ACAACACCTGAGAACAGAAGCAGGA-3. To target *p53* expression, we used a previously characterized morpholino (Langheinrich et al., 2002). To control for phenotypes resulting from the injection procedure alone, a standard control morpholino that has no target or biological activity within the zebrafish was used in all experiments (Gene Tools). Phenotypes between standard morphants and those injected with the 5-bp mismatch *chd7* morpholino were comparable. Zebrafish embryos received 2.5 ng of *chd7* morpholino, 5 ng of standard control morpholino, 4 ng *p53* morpholino, or 5 ng *fbxl10* morpholino unless concentration is indicated otherwise. The *chd7*/*fbxl10* double morphants received a simultaneous injection of 2.5 ng *chd7* morpholino and 5 ng *fbxl10* morpholino. The *chd7*/*p53* double morphants received a simultaneous injection of 2.5 ng *chd7* morpholino and 4 ng *p53* morpholino. This *p53* morpholino dosage was slightly higher than that recommended for testing for non-specific morpholino related cell death (Robu et al., 2007). For all co-injection experiments, *chd7* and *fbxl10* or *chd7* and *p53* morpholino single injections were performed in parallel as an additional control. All morpholinos were designed and manufactured by Gene Tools (Philomath, Oregon). Morpholinos were dissolved in sterile water to stock solution of 65 mg/ml. 5 mg/ml or 10 mg/ml working solutions were made by diluting the morpholino in water and 2% phenyl red. Zebrafish embryos were then injected at the 1 or 2 cell stage with using a microinjector.

Scoring of zebrafish morphant phenotypes

Zebrafish embryos were incubated at 28 °C in fish water until the desired developmental stage was reached. The *chd7* morphant phenotypes were monitored and scored using a Leica S6E stereomicroscope between 4 and 6 dpf. The bright-field images of *chd7* morphant phenotypes were taken at 6 dpf and were images on a Leica DM6000. Significance was assessed by chi-square contingency test.

RNA extraction, cDNA synthesis, and qRT-PCR

Total RNA was extracted by homogenizing 20–30 pooled embryos at 8 hpf or 25 hpf in Trizol reagent (Invitrogen). Embryos were homogenized by drawing them through a 21G 1½ needle and 1 ml syringe (BD) approximately 20 times. RNA was further purified via the Trizol Reagent protocol (Invitrogen) and was re-dissolved in RNase-free water. From the total purified RNA, cDNA was synthesized using a High-capacity cDNA Archive Kit (Applied Biosystems). Using quantitative polymerase-chain reaction (PCR), gene expression was measured in triplicates across a set of three biological replicates. PCR reactions were performed using Sybr-Green or Taqman chemistry on an ABI 7300 real-time thermocycler. Designed primer sequences for PCR reactions are listed in Table 2. Expression of the 45S rRNA transcript measured using a previously published primer set (Azuma et al., 2006). Expression of several genes was amplified using several Taqman assays (Invitrogen) including *p27* (ID: Dr03101119_ml) and *β-actin1* (ID: Dr0332610_m1). Permission for the *ink4ab* Taqman probe (ID: AJ1RUB6) was provided graciously by Dr. Hatem Sabaawy.

Cartilage staining of whole mounts

At 4 dpf, zebrafish were anesthetized with tricaine and fixed with cold 4% paraformaldehyde solution (PFA). Zebrafish cartilage was stained with Alcian blue and Alzarian Red as previously described (Walker and Kimmel, 2007). Zebrafish were imaged in glycerol and bright-field images were taken using a Leica MZ10F fluorescent microscope.

Cartilage sectioning

Zebrafish morphants were anesthetized with tricaine and fixed with cold 4% PFA at 4 dpf. The sample preparation, sectioning, and Alcian blue staining of all zebrafish embryos were performed by Histoserv, Inc. (Germantown, MD). All embryos were sectioned at 10 μm.

Whole-mount antibody labeling

At 25 hpf, zebrafish embryos were anesthetized with tricaine and fixed with cold 4% PFA overnight at 4 °C. Fixed embryos were rinsed several times with PBS and permeablilized overnight at room temperature with 3% Triton in PBS. Embryos were rinsed in PBS again and blocked in 5% normal goat serum in PBS (blocking solution) for 3 h at room temperature. Embryos were then incubated with rabbit anti-phosphorylated Histone H3 (phospho-ser10) antibody (1:200, Cell Signal #9701) diluted in blocking solution overnight at 4 °C. Embryos were rinsed several times over 6 h in blocking solution and incubated overnight at 4 °C with goat anti-rabbit AlexaFluor 488 (1:200, Invitrogen A-11008). Embryos were rinsed in blocking solution for 2 h. Zebrafish were stored in VECTASHIELD mounting medium (VECTOR Laboratories). Fluorescent images were taken on a Leica MZ10F microscope after mounting zebrafish in 0.1% agarose.

Quantification of proliferation

Quantification of the cellular area expressing fluorescently labeled P-H3 was performed using Adobe Photoshop as previously described (Lehr et al., 1999). Mitotic cells were quantified by calculating the average fluorescent area (pixel^2). Five cells within each fluorescent image were selected using the Photoshop Magic Wand Tool. On selection of the five mitotic cells, cells of similar fluorescent intensity were selected using the "Select Similar" command with a stringency factor of 20. Cells were not selected

for based on intensity; however, selected cells in the plane of focus tended to be slightly higher in fluorescent intensity. The average pixel area was calculated for each image and the process was repeated across three separate z-planes for each zebrafish embryo. The three averaged pixel areas from the z-planes were again averaged to give a total average pixel area for each individual embryo. The total average pixel areas from multiple zebrafish embryos were plotted and statistical significance was determined using a Student's t-test.

To count the number of P-H3-positive cells, zebrafish embryos were imaged on a Leica SP2 confocal microscope. Z-plane images were taken throughout the embryo at 40 μm steps to avoid capturing cells in multiple z-planes. The cells were then manually counted by an individual who was blind to the identity of the morpholino used in the experiment, to avoid bias. The data were then stratified by the morpholino used (Standard versus chd7), and the results were plotted and tested for statistical significance using a Student's two-tailed t-test.

Acknowledgments

Appendix A. Supporting information

Supplementary data associated with this article can be found in the online version at http://dx.doi.org/10.1016/j.ydbio.2013.07.026.

References

Altschul, S.F., Madden, T.L., Schaffer, A.A., Zhang, J., Zhang, Z., Miller, W., Lipman, D. J., 1997. Gapped BLAST and PSI-BLAST: a new generation of protein database search programs. Nucleic Acids Res. 25, 3389–3402.

Azuma, M., Toyama, R., Laver, E., Dawid, I.B., 2006. Perturbation of rRNA synthesis in the bap28 mutation leads to apoptosis mediated by p53 in the zebrafish central nervous system. J. Biol. Chem. 281, 13309–13316.

Bajpai, R., Chen, D.A., Rada-Iglesias, A., Zhang, J., Xiong, Y., Helms, J., Chang, C.P., Zhao, Y., Swigut, T., Wysocka, J., 2010. CHD7 cooperates with PBAF to control multipotent neural crest formation. Nature 463, 958–962.

Bartels, C.F., Scacheri, C., White, L., Scacheri, P.C., Bale, S., 2010. Mutations in the CHD7 gene: the experience of a commercial laboratory. Genet. Test. Mol. Biomarkers 14, 881–891.

Bosman, E.A., Penn, A.C., Ambrose, J.C., Kettleborough, R., Stemple, D.L., Steel, K.P., 2005. Multiple mutations in mouse Chd7 provide models for CHARGE syndrome. Hum. Mol. Genet. 14, 3463–3476.

Cole, P.A., 2008. Chemical probes for histone-modifying enzymes. Nat. Chem. Biol. 4, 590–597.

Dauwerse, J.G., Dixon, J., Seland, S., Ruivenkamp, C.A., van Haeringen, A., Hoefsloot, L.H., Peters, D.J., Boers, A.C., Daumer-Haas, C., Maiwald, R., et al., 2011. Mutations in genes encoding subunits of RNA polymerases I and III cause Treacher Collins syndrome. Nat. Genet. 43, 20–22.

Edwards, S.J., Gladwin, A.J., Dixon, M.J., 1997. The mutational spectrum in Treacher Collins syndrome reveals a predominance of mutations that create a premature-termination codon. Am. J. Hum. Genet. 60, 515–524.

Engelen, E., Akinci, U., Bryne, J.C., Hou, J., Gontan, C., Moen, M., Szumska, D., Kockx, C., van Ijcken, W., Dekkers, D.H., et al., 2011. Sox2 cooperates with Chd7 to regulate genes that are mutated in human syndromes. Nat. Genet. 43, 607–611.

Feng, W., Yonezawa, M., Ye, J., Jenuwein, T., Grummt, I., 2010. PHF8 activates transcription of rRNA genes through H3K4me3 binding and H3K9me1/2 demethylation. Nat. Struct. Mol. Biol. 17, 445–450.

Frescas, D., Guardavaccaro, D., Bassermann, F., Koyama-Nasu, R., Pagano, M., 2007. JHDM1B/FBXL10 is a nucleolar protein that represses transcription of ribosomal RNA genes. Nature 450, 309–313.

Fukuda, T., Tokunaga, A., Sakamoto, R., Yoshida, N., 2011. Fbxl10/Kdm2b deficiency accelerates neural progenitor cell death and leads to exencephaly. Mol. Cell. Neurosci. 46, 614–624.

Gladwin, A.J., Dixon, J., Loftus, S.K., Edwards, S., Wasmuth, J.J., Hennekam, R.C., Dixon, M.J., 1996. Treacher Collins syndrome may result from insertions, deletions or splicing mutations, which introduce a termination codon into the gene. Hum. Mol. Genet. 5, 1533–1538.

Hall, J.A., Georgel, P.T., 2007. CHD proteins: a diverse family with strong ties. Biochem. Cell Biol. 85, 463–476.

He, J., Kallin, E.M., Tsukada, Y., Zhang, Y., 2008. The H3K36 demethylase Jhdm1b/Kdm2b regulates cell proliferation and senescence through p15(Ink4b). Nat. Struct. Mol. Biol. 15, 1169–1175.

Holzel, M., Rohrmoser, M., Schlee, M., Grimm, T., Harasim, T., Malamoussi, A., Gruber-Eber, A., Kremmer, E., Hiddemann, W., Bornkamm, G.W., et al., 2005. Mammalian WDR12 is a novel member of the Pes1-Bop1 complex and is required for ribosome biogenesis and cell proliferation. J. Cell Biol. 170, 367–378.

Hurd, E.A., Capers, P.L., Blauwkamp, M.N., Adams, M.E., Raphael, Y., Poucher, H.K., Martin, D.M., 2007. Loss of Chd7 function in gene-trapped reporter mice is embryonic lethal and associated with severe defects in multiple developing tissues. Mamm. Genome: Off. J. Int. Mamm. Genome Soc. 18, 94–104.

Hurd, E.A., Poucher, H.K., Cheng, K., Raphael, Y., Martin, D.M., 2010. The ATP-dependent chromatin remodeling enzyme CHD7 regulates pro-neural gene expression and neurogenesis in the inner ear. Development 137, 3139–3150.

Jacobs-McDaniels, N.L., Albertson, R.C., 2011. Chd7 plays a critical role in controlling left-right symmetry during zebrafish somitogenesis. Dev. Dyn. 240, 2272–2280.

Janssen, N., Bergman, J.E., Swertz, M.A., Tranebjaerg, L., Lodahl, M., Schoots, J., Hofstra, R.M., van Ravenswaaij-Arts, C.M., Hoefsloot, L.H., 2012. Mutation update on the CHD7 gene involved in CHARGE syndrome. Hum. Mutat. 33, 1149–1160.

Jones, N.C., Lynn, M.L., Gaudenz, K., Sakai, D., Aoto, K., Rey, J.P., Glynn, E.F., Ellington, L., Du, C., Dixon, J., et al., 2008. Prevention of the neurocristopathy Treacher Collins syndrome through inhibition of p53 function. Nat. Med. 14, 125–133.

Jongmans, M.C., Admiraal, R.J., van der Donk, K.P., Vissers, L.E., Baas, A.F., Kapusta, L., van Hagen, J.M., Donnai, D., de Ravel, T.J., Veltman, J.A., et al., 2006. CHARGE syndrome: the phenotypic spectrum of mutations in the CHD7 gene. J. Med. Genet. 43, 306–314.

Kague, E., Gallagher, M., Burke, S., Parsons, M., Franz-Odendaal, T., Fisher, S., 2012. Skeletogenic fate of zebrafish cranial and trunk neural crest. PLoS One 7, e47394.

Kita, Y., Nishiyama, M., Nakayama, K.I., 2012. Identification of CHD7S as a novel splicing variant of CHD7 with functions similar and antagonistic to those of the full-length CHD7L. Genes Cells: Devoted Mol. Cell. Mech. 17, 536–547.

Knight, R.D., Schilling, T.F., 2006. Cranial neural crest and development of the head skeleton. Adv. Exp. Med. Biol. 589, 120–133.

Lalani, S.R., Safiullah, A.M., Fernbach, S.D., Harutyunyan, K.G., Thaller, C., Peterson, L. E., McPherson, J.D., Gibbs, R.A., White, L.D., Hefner, M., et al., 2006. Spectrum of CHD7 mutations in 110 individuals with CHARGE syndrome and genotype-phenotype correlation. Am. J. Hum. Genet. 78, 303–314.

Langheinrich, U., Hennen, E., Stott, G., Vacun, G., 2002. Zebrafish as a model organism for the identification and characterization of drugs and genes affecting p53 signaling. Curr. Biol. 12, 2023–2028.

Layman, W.S., McEwen, D.P., Beyer, L.A., Lalani, S.R., Fernbach, S.D., Oh, E., Swaroop, A., Hegg, C.C., Raphael, Y., Martens, J.R., et al., 2009. Defects in neural stem cell proliferation and olfaction in Chd7 deficient mice indicate a mechanism for hyposmia in human CHARGE syndrome. Hum. Mol. Genet. 18, 1909–1923.

Layman, W.S., Hurd, E.A., Martin, D.M., 2011. Reproductive dysfunction and decreased GnRH neurogenesis in a mouse model of CHARGE syndrome. Hum. Mol. Genet. 20, 3138–3150.

Lehr, H.A., van der Loos, C.M., Teeling, P., Gown, A.M., 1999. Complete chromogen separation and analysis in double immunohistochemical stains using Photoshop-based image analysis. J. Histochem. Cytochem.: Off. J. Histochem. Soc. 47, 119–126.

Li, J., Santoro, R., Koberna, K., Grummt, I., 2005. The chromatin remodeling complex NoRC controls replication timing of rRNA genes. EMBO J. 24, 120–127.

Lohse, B., Kristensen, J.L., Kristensen, L.H., Agger, K., Helin, K., Gajhede, M., Clausen, R.P., 2011. Inhibitors of histone demethylases. Bioorg. Med. Chem. 19, 3625–3636.

Marchler-Bauer, A., Lu, S., Anderson, J.B., Chitsaz, F., Derbyshire, M.K., DeWeese-Scott, C., Fong, J.H., Geer, L.Y., Geer, R.C., Gonzales, N.R., et al., 2011. CDD: a Conserved Domain Database for the functional annotation of proteins. Nucleic Acids Res. 39, D225–D229.

McStay, B., Grummt, I., 2008. The epigenetics of rRNA genes: from molecular to chromosome biology. Annu. Rev. Cell Dev. Biol. 24, 131–157.

Narla, A., Ebert, B.L., 2010. Ribosomopathies: human disorders of ribosome dysfunction. Blood 115, 3196–3205.

Patten, S.A., Jacobs-McDaniels, N.L., Zaouter, C., Drapeau, P., Albertson, R.C., Moldovan, F., 2012. Role of Chd7 in zebrafish: a model for CHARGE syndrome. PLoS One 7, e31650.

Pestov, D.G., Strezoska, Z., Lau, L.F., 2001. Evidence of p53-dependent cross-talk between ribosome biogenesis and the cell cycle: effects of nucleolar protein Bop1 on G(1)/S transition. Mol. Cell Biol. 21, 4246–4255.

Randall, V., McCue, K., Roberts, C., Kyriakopoulou, V., Beddow, S., Barrett, A.N., Vitelli, F., Prescott, K., Shaw-Smith, C., Devriendt, K., et al., 2009. Great vessel development requires biallelic expression of Chd7 and Tbx1 in pharyngeal ectoderm in mice. J. Clin. Invest. 119, 3301–3310.

Rauch, G.J., Lyons, D.A., Middendorf, I., Friedlander, B., Arana, N., Reyes, T., Talbot, W. S., 2003. Submission and Curation of Gene Expression Data. ZFIN Direct Data Submission.

Robu, M.E., Larson, J.D., Nasevicius, A., Beiraghi, S., Brenner, C., Farber, S.A., Ekker, S. C., 2007. p53 activation by knockdown technologies. PLoS Genet. 3, e78.

Sabaawy, H.E., Azuma, M., Embree, L.J., Tsai, H.J., Starost, M.F., Hickstein, D.D., 2006. TEL-AML1 transgenic zebrafish model of precursor B cell acute lymphoblastic leukemia. Proc. Natl. Acad. Sci. USA 103, 15166–15171.

Sanlaville, D., Etchevers, H.C., Gonzales, M., Martinovic, J., Clement-Ziza, M., Delezoide, A.L., Aubry, M.C., Pelet, A., Chemouny, S., Cruaud, C., et al., 2006. Phenotypic spectrum of CHARGE syndrome in fetuses with CHD7 truncating mutations correlates with expression during human development. J. Med. Genet. 43, 211–217.

Schnetz, M.P., Bartels, C.F., Shastri, K., Balasubramanian, D., Zentner, G.E., Balaji, R., Zhang, X., Song, L., Wang, Z., Laframboise, T., et al., 2009. Genomic distribution of CHD7 on chromatin tracks H3K4 methylation patterns. Genome Res. 19, 590–601.

Schnetz, M.P., Handoko, L., Akhtar-Zaidi, B., Bartels, C.F., Pereira, C.F., Fisher, A.G., Adams, D.J., Flicek, P., Crawford, G.E., Laframboise, T., et al., 2010. CHD7 targets active gene enhancer elements to modulate ES cell-specific gene expression. PLoS Genet. 6, e1001023.

Siebert, J.R., Graham Jr., J.M., MacDonald, C., 1985. Pathologic features of the CHARGE association: support for involvement of the neural crest. Teratology 31, 331–336.

Thisse, B., Thisse, C., 2004. Fast Release Clones: A High Throughput Expression Analysis. ZFIN Direct Data Submission.

Tian, C., Yu, H., Yang, B., Han, F., Zheng, Y., Bartels, C.F., Schelling, D., Arnold, J.E., Scacheri, P.C., Zheng, Q.Y., 2012. Otitis media in a new mouse model for CHARGE syndrome with a deletion in the Chd7 gene. PLoS One 7, e34944.

Tzatsos, A., Pfau, R., Kampranis, S.C., Tsichlis, P.N., 2009. Ndy1/KDM2B immortalizes mouse embryonic fibroblasts by repressing the Ink4a/Arf locus. Proc. Natl. Acad. Sci. USA 106, 2641–2646.

Tzatsos, A., Paskaleva, P., Lymperi, S., Contino, G., Stoykova, S., Chen, Z., Wong, K.K., Bardeesy, N., 2011. Lysine-specific demethylase 2B (KDM2B)-let-7-enhancer of zester homolog 2 (EZH2) pathway regulates cell cycle progression and senescence in primary cells. J. Biol. Chem. 286, 33061–33069.

Vissers, L.E., van Ravenswaaij, C.M., Admiraal, R., Hurst, J.A., de Vries, B.B., Janssen, I. M., van der Vliet, W.A., Huys, E.H., de Jong, P.J., Hamel, B.C., et al., 2004. Mutations in a new member of the chromodomain gene family cause CHARGE syndrome. Nat. Genet. 36, 955–957.

Walker, M.B., Kimmel, C.B., 2007. A two-color acid-free cartilage and bone stain for zebrafish larvae. Biotechnic Histochem.: Off. Publ. Biol. Stain Comm. 82, 23–28.

Zentner, G.E., Layman, W.S., Martin, D.M., Scacheri, P.C., 2010a. Molecular and phenotypic aspects of CHD7 mutation in CHARGE syndrome. Am. J. Med. Genet. A 152A, 674–686.

Zentner, G.E., Hurd, E.A., Schnetz, M.P., Handoko, L., Wang, C., Wang, Z., Wei, C., Tesar, P.J., Hatzoglou, M., Martin, D.M., et al., 2010b. CHD7 functions in the nucleolus as a positive regulator of ribosomal RNA biogenesis. Hum. Mol. Genet. 19, 3491–3501.